

24TH INTERNATIONAL WORKSHOP ON RADIATION IMAGING DETECTORS
OSLO, NORWAY
25–29 JUNE 2023

Balancing gain and dynamic range in a 25 μm pitch hybrid pixel detector

J. Heymes,* R. Barten, F. Baruffaldi, A. Bergamaschi, M. Brückner, M. Carulla, R. Dinapoli, S. Ebner, E. Fröjd, D. Greiffenberg, S. Hasanaj, V. Hinger, T. King, P. Kozłowski, C. Lopez-Cuenca, D. Mezza, K. Moustakas, A. Mozzanica, K.A. Paton, C. Ruder, B. Schmitt, D. Thattil, X. Xie and J. Zhang

PSD Detector Group, Paul Scherrer Institut,
Forschungsstrasse 111, 5232 Villigen PSI, Switzerland

E-mail: julian.heymes@psi.ch

ABSTRACT: MÖNCH is a hybrid pixel detector featuring 25 μm pixel pitch and analogue readout for X-ray imaging at synchrotron radiation (SR) facilities. Sub-pixel spatial resolution has been demonstrated using charge sharing and interpolation algorithms. The current prototype version, MÖNCH0.4, features 19 different pixel architectures to assess the design choices and components for an optimised architecture to be used at SR facilities, and to explore the potential use of dynamic gain switching in fine pitch pixels for applications at X-ray free electron lasers (XFELs).

Previous characterisation results of the pixel architectures without dynamic gain switching have shown noise levels as low as 21.7 e^- r.m.s., which have now been pushed to sub-20 e^- r.m.s at room temperature using standard 300 μm -thick silicon sensors. Achieving low noise values however requires high conversion gain and necessitates design choices such as the simplification of the pixel architecture (e.g. by limiting the available choice of in-pixel gains). These compromises ultimately restrain the available dynamic range and prevent the use of MÖNCH with low-gain avalanche diodes (LGADs) or high-Z sensors because of the large signals (internal amplification and high photon energies, respectively) and of large leakage currents.

In this paper, we will introduce the MÖNCH project followed by a description of the current prototype along with characterisation results of the pixel architectures without dynamic gain switching for synchrotron applications with an emphasis on noise and dynamic range. These experimental results will be used to fine-tune the design of MÖNCH0.5 to validate the final pixel design. This small prototype should also include additional features from the continuous developments of the PSD detector group towards a full-scale $2 \times 3 \text{ cm}^2$ MÖNCH1.0.

KEYWORDS: Front-end electronics for detector readout; Hybrid detectors; X-ray detectors

*Corresponding author.



Contents

1	Introduction	1
2	The MÖNCH0.4 ASIC	2
2.1	Design and floorplan	2
2.2	Static gain pixels	3
3	Laboratory characterisation of MÖNCH0.4	4
3.1	X-ray calibration	4
3.2	Noise	4
3.3	X-ray detection performance	5
3.4	Gain and linearity	5
3.5	Evaluation of the dynamic range	6
3.6	Noise and dynamic range	7
4	Conclusions and the future of MÖNCH	7

1 Introduction

MÖNCH (Micropixel with enhanced position resolution using charge integration) is a charge integrating hybrid pixel detector (HPD) with 25 μm pitch pixel and analogue readout. One of the main challenges of small pixels in HPDs is the very limited area available for the front-end design, therefore requiring design trade-offs for optimal performance. However, the use of small pixel pitch benefits from lower dark current, lower input capacitance and high native spatial resolution that can be enhanced exploiting the effects of charge sharing [1].

In the standard sensors (fully depleted 320 μm thick n-type silicon, biased at 120 V), the diameter of the charge cloud generated from an absorbed X-ray photon is of the order of 10 μm [1]. It is therefore very likely that the charge will be shared over several pixels. With low fluxes (approx. 1 % occupancy), isolated photons can be detected and identified as clusters of 2 x 2 pixels. The analogue output of all pixels in the cluster, which is proportional to the charge in the same pixel, can be summed to reconstruct the total cluster charge and therefore the energy of the impinging photon. The energy resolution is given by the electronic noise, scaled with the square root of the number of pixels of the cluster. Moreover, charge sharing can be exploited to reconstruct the position of the impinging photon with a resolution of the order of a few microns, almost an order of magnitude better than the physical pixel size [2].

The use of MÖNCH with static gains and low noise for single photon detection is of great interest for experiments using X-ray tubes or for photon starved applications at synchrotron beamlines (e.g., energy dispersive spectrometers). There, the detector must be operated at high frame rates (above 1 kHz) with parallel exposure and readout to optimize the duty cycle. At brighter synchrotron

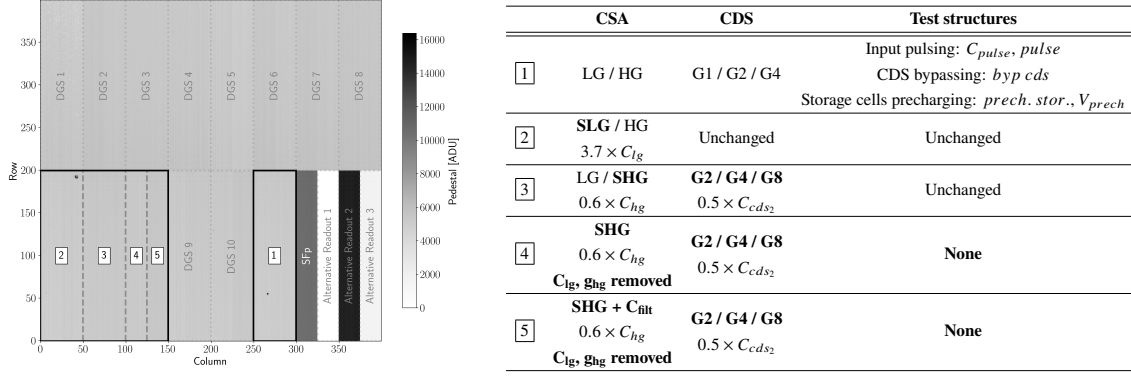


Figure 1. Left: pedestal map of MÖNCH0.4 showing the 19 different pixel architectures. Right: features summary of the static gain pixel architectures implemented in MÖNCH0.4, with the changes from the reference architecture **1** marked in bold.

beamlines a pixel design with static gain optimised for high dynamic range (with single photon detection capabilities) can be used to integrate several photons, resulting in a 25 μm resolution image without energy resolution.

For experiments at X-ray free electron lasers (XFELs), the photon flux can reach up to several thousand photons per pixel per bunch, requiring Dynamic Gain Switching (DGS) to keep the electronic noise below the statistical fluctuations on the number of photons. In this case, very short exposure times can be used (approx. 10 μs , as the typical bunches are extremely short) with relaxed frame rates to cope with the repetition rate of the machine (e.g. 100 Hz at SwissFEL). Examples of possible applications for MÖNCH include: (in-vivo) tomography [3], resonant inelastic X-ray scattering (RIXS) [4], Fourier ptychography [5], G2-less interferometry [6], high resolution imaging [7], colour imaging [7], electron microscopy [8].

After the successful testing of several MÖNCH prototypes [9, 10] a new large area prototype MÖNCH0.4 consisting in 400×400 pixels with 19 different pixel architectures has been designed and produced in order to test different solutions with and without dynamic gain switching and select the most promising ones. The different MÖNCH0.4 pixel architectures are described in details in section 2. The laboratory characterisation results of this latest ASIC are presented in section 3 with an emphasis on the dynamic range.

2 The MÖNCH0.4 ASIC

2.1 Design and floorplan

Like MÖNCH0.3 [10], the matrix features 400×400 pixels (1 cm^2) but is separated in 19 pixel designs to explore gain and noise performance with both static gain and dynamic gain switching, and alternative readout schemes. A dark image of a MÖNCH0.4 readout chip bump-bonded to a 300 μm thick silicon sensor is shown in figure 1 left. The different architectures are delimited and independently labeled. Each pixel design covers 200 rows and at least 25 columns (1 supercolumn), up to 50 columns (2 supercolumns). The bottom right of the chip contains 3 architectures with alternative readout schemes and one design based on only one source-follower. The top part of

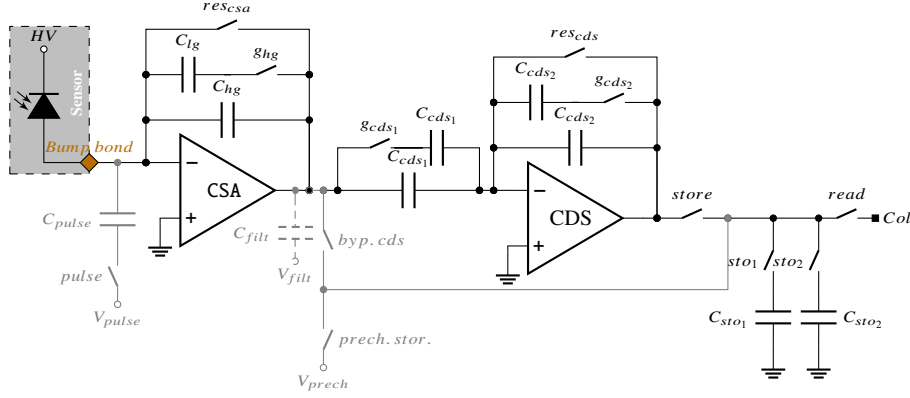


Figure 2. Simplified block schematic of the static gain pixel designs implemented in MÖNCH0.4. The signal is amplified through a charge sensitive preamplifier and a correlated double sampling stage. The amplified and filtered signal is stored in the storage cells for readout. The gain of each stage is statically set. Depending on the design, additional testing elements can be implemented (solid grey lines) as well as an extra filtering capacitor at the output of the CSA (dashed grey lines).

MÖNCH0.4 only features 8 architectures with DGS. Two more DGS designs are present in the middle bottom part. The 5 remaining variations are the statically selectable gain architectures characterised in this work and described in figure 1 right.

2.2 Static gain pixels

The 5 architectures with static gains share a common design baseline shown as a simplified schematic in figure 2. The sensor is bump-bonded to the input of the charge sensitive preamplifier (CSA) where its gain is related to the total capacitance of the feedback loop ($G_{csa} = 1/C_f$). The gain can be either set to high gain (g_{hg} open, $C_f = C_{hg}$) or to low gain (g_{hg} closed, $C_f = C_{lg} + C_{hg}$). The preamplifier can be reset using res_{csa} . For one of the architectures, an additional capacitor is added at the output of the CSA to act as an additional filter (shown as a greyed dashed line).

The amplified signal then passes through a correlated double sampling (CDS) stage where it is further amplified. The gain of the CDS can be statically set to any of the three accessible gains by combining the capacitors at the input and in the feedback using the g_{cds1} and g_{cds2} switches. The CDS stage can also be reset. The output of the CDS can be stored on either or both storage capacitors (one metal-to-metal capacitor, one transistor capacitor with equivalent capacitance). Finally the stored value can be read-out via a source-follower through a common column bus (not represented on the schematic).

Additional features are implemented in some architectures for further testability of the front-end designs (all shown as grey solid lines in the schematic). The signal generated by the collection of a photon can be emulated by pulsing an injection capacitor connected at the input node of the CSA. The CDS stage can be bypassed to directly probe the output of the CSA. Finally, it is possible to precharge the storage cells using an external voltage. More testing features are implemented in the whole readout chain and will not be described further here. The details of the five static gain architectures are summarised in the table in figure 1 right.

In the table, all the designs are compared to a reference ([1]), which is based on the pixel design of MÖNCH0.3. This reference design features two selectable preamp gains (Low gain and high gain) and three selectable CDS gains (G1, G2, G4). All the test features have been implemented and the filter after the CSA is not present. The super low gain architecture ([2]) is similar at the exception that the low gain capacitor of the CSA (C_{lg}) is $3.7 \times$ larger than the reference, providing a reduced low gain (SLG). Oppositely, the super high gain configuration (SHG, [3]) features a smaller high gain capacitance in the CSA ($0.6 \times$ the reference) while C_{lg} remains unchanged. The value of the capacitors in the feedback loop of the CDS stage are halved, therefore doubling all the CDS gains. The two remaining designs ([4] and [5]) feature the same changes as in [3] but are stripped into a minimal configuration. The low gain branch with the gain switch of the CSA has been completely removed. All the test structures have also been removed. The only difference between the stripped SHG architectures is the additional filtering capacitor after the CSA in [5] to observe its effect on noise performance.

3 Laboratory characterisation of MÖNCH0.4

A MÖNCH0.4 detector has been tested in the PSI laboratories to determine its performance using the Chip Test Board (CTB). This readout system provides full control over the digital patterns and the biases applied to the chip. The system was water-cooled to about 18°C (water temperature) to guarantee constant performance over time. The chip was readout at 1 kHz via a 10 GbE optical link and the exposure time was set to $1\ \mu\text{s}$ unless explicitly stated otherwise.

3.1 X-ray calibration

The MÖNCH0.4 detector has been calibrated with fluorescence X-rays. The source is an X-ray tube with a tungsten anode operated at 20 kV and 80 mA. The beam is oriented towards an iron target whose fluorescence photons ($\text{Fe-K}_\alpha = 6.403\ \text{keV}$, $\text{Fe-K}_\beta = 7.057\ \text{keV}$) arrive on the detector oriented at 90° with respect to the X-ray tube. The settings and distance between the target and the detector were tuned to guarantee low occupancy. A set of 1,000,000 frames was acquired on which the photon finding algorithm described in [2] has been applied after pedestal subtraction from the acquisition of 1000 consecutive dark frames to extract each event into clusters. The 2×2 clusters spectra for each pixel design has been reconstructed and is shown in figure 3 left. The position of the Fe-K_α peak is used to calibrate the gain of the detector to assess noise and linearity.

3.2 Noise

The noise was assessed using the set of 1000 consecutive dark frames. The mean image provides the pedestal and is used for baseline subtraction. The per-pixel r.m.s. noise was also computed from this data-set and was converted to electrons using X-ray calibrations results (section 3.1). The noise distributions for the 5 static gain pixel architectures at their maximum gain settings is shown in figure 3 right.

The noise of the reference design ([1], $30.64\ \text{e}^-$) is similar to the measured value in MÖNCH0.3. For [2], the noise is also equivalent, as expected, as the high gain configuration is similar. The remaining architectures all feature a large increase in gain, resulting in a notable improvement of the noise performance. For [3] the noise reaches $20.69\ \text{e}^-$. With the low gain branch of the CSA and the testing

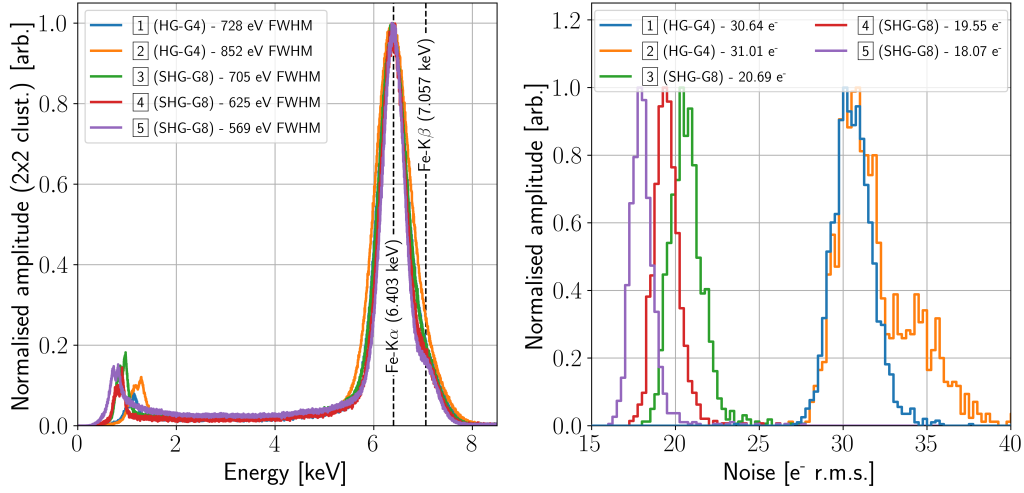


Figure 3. Left: iron fluorescence spectra for the static gain pixel architectures of MÖNCH0.4 at their respective highest gain settings. Right: noise distribution of the static gain pixel architectures of MÖNCH04. The gain is set to the highest settings for both the preamplifier and the CDS in all the architectures.

capabilities removed in [4], thus removing the corresponding parasitic capacitors connected with the input node of the CSA, a further improvement in performance is observed (19.55 e⁻). It is unfortunately impossible to disentangle the contribution of each element, but this hints that keeping the architecture to its bare minimum is needed for minimum noise operation. Finally, with the extra filtering capacitor at the output of the CSA in [5], an additional improvement in noise is observed (18.07 e⁻).

3.3 X-ray detection performance

For the pixel design with the worst noise performance ([2]) the measured energy resolution at Fe-K α is 852 eV FWHM (13.3%). A significant improvement is observed for the design with the lowest noise ([5]): 569 eV FWHM (8.9%). Overall, with the reduction of noise as the calibration peak shrinks, the Fe-K β peak becomes discernible. It is worth noting that the spectra are for 2 × 2 clusters where the total noise is twice the single pixel value.

At the same time, the noise peak at the baseline shrinks, allowing the detection of lower energy single photons. The minimum detectable energy ($5\sigma_{2 \times 2 \text{ clusters}}$) with single photon resolution for [2] would be around 1.5 keV, and around 1 keV for [5]. Below these limits, sensors with internal gain such as LGADs are necessary [11].

3.4 Gain and linearity

The X-ray calibration method presented in section 3.1 has been repeated with different fluorescence materials: Ti (4.510 keV), Cu (8.407 keV), and Mo (17.478 keV). The measured peak position against photon energy for each architecture is shown in figure 4. Each dataset has been fitted with an affine function to determine the gain. Finally, the residuals are shown as an indication of non-linearities.

The gains of the standard configurations ([1], [2]) are similar. However for the super high gain variants ([3], [4], and [5]), the gains are notably different ($\approx 7.5\%$) between both stripped versions and the standard one. This difference could be attributed to parasitics; more precisely to the low gain

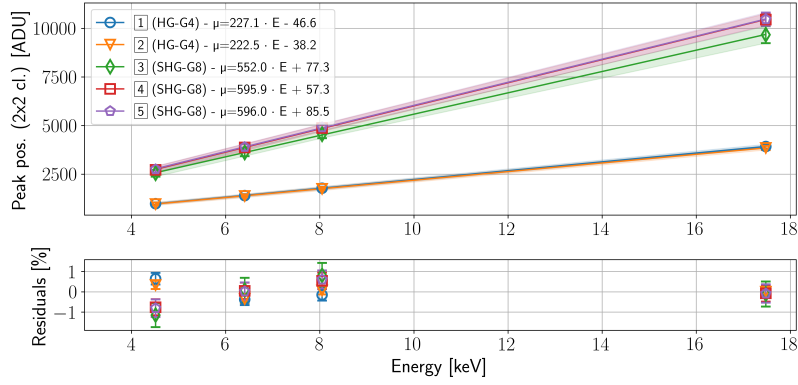


Figure 4. Top: energy calibration of the static gain pixels of MÖNCH0.4 at their highest gain settings for 4 different energies: Ti (4.510 keV), Fe (6.409 keV), Cu (8.407 keV), and Mo (17.478 keV). The gain is obtained from the fitting of the points. Bottom: residuals of the fit.

branch of the CSA adding capacitance and therefore reducing the gain. This result once again points towards the necessity to minimise the parasitics and optimise the layout in the designs.

About 1 % non-linearities can be observed at the lower end of the tested energy range. It would be of prime interest to extend the measurements to lower photon energies to correctly assess the linearity in the single photon operating range. On the other end of the range, optical photons can be integrated to emulate large signals as the silicon sensor used would become transparent to higher energy photons.

3.5 Evaluation of the dynamic range

Evaluating the dynamic range requires reaching the saturation of the system. The dynamic range has therefore been evaluated using a laser in the optical range. In order to detect optical photons, the aluminium coating on the backside of a sensor has been etched away. The spot of a near-infrared laser ($\lambda = 1000\text{--}1100\text{ nm}$) has then been focused within a single pixel. The intensity of the integrated signal was modulated by pulsing (0–100 times, 100 ns period). The exposure time of the readout was set to 10 μs . The maximum intensity of the signal (i.e. around 100 pulses) was modulated using a combination of neutral density filters. The filter power has been tuned for each gain configuration and design to reach saturation from a few pulses below 100. For each configuration, 1000 frames have been acquired. The mean input signal is converted to a charge using X-ray calibrations. The pedestal corrected signal against the input charge for the static gain designs for all configurations of CSA and CDS gains is shown in figure 5.

The maximum measured charge is inversely proportional to the gain. The response in the stripped SHG pixels ([4], and [5]) has been measured with the other front ends configured in either low gain or high gain. No noticeable effect can be observed from either of the global gain configuration. The measurements over the entire dynamic range have uncovered larger non-linearities at higher signals (above the signal generated by a single 17.478 keV photon in [4] and [5]). Our investigations determined that these effects are very likely originating from the column-level buffer which will be improved in subsequent designs. The contributions have been included in the errors calculations. The evaluation of the dynamic range is performed at the intersection between the low end of the errors and the saturation levels as shown in figure 5 left with + markers for [1].

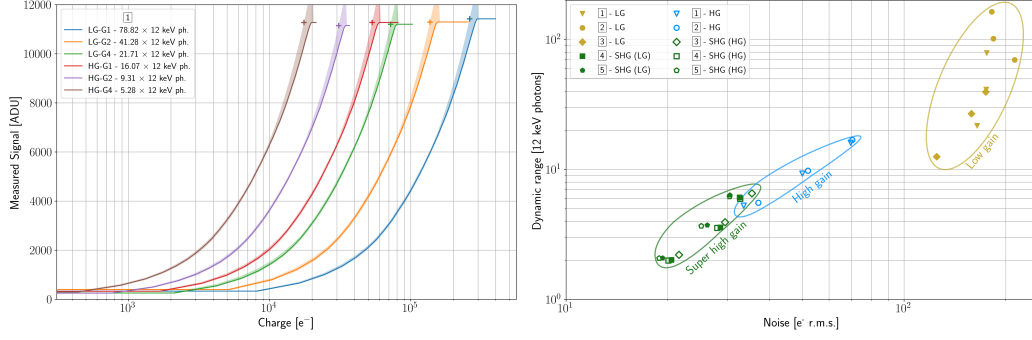


Figure 5. Left: measured signal obtained from a pulsed laser source at all gain settings for the architecture 1 of MÖNCH0.4. The charge corresponding to the dynamic range is marked using + markers. Right: scatter plot of the dynamic range (as a number of 12 keV photons) against the measured noise for all the possible gain settings of the static gain pixel designs of MÖNCH0.4.

3.6 Noise and dynamic range

The charge corresponding to the dynamic range for each parameter tested is converted to an equivalent number of 12 keV photons (3315 e^- /ph.). The measured value is plotted against the calibrated noise for each architecture and gain configuration in figure 5 right.

Two main regions can be seen: low gain, and high gain which can also be separated in two halves (high gain and super high gain). The low gain configuration offers very high dynamic range (up to 163×12 keV photons) at the expense of noise (181 e^- r.m.s.). On the opposite, the high gain offers low noise performance (18–70 e^- r.m.s) with a limited dynamic range (2–17 $\times 12$ keV photons). No outliers that offer both low noise and higher dynamic range can be seen proving that for these pixel architectures, the noise performance is directly linked to the gain of the front-end.

4 Conclusions and the future of MÖNCH

The measurements conducted on five different architectures with statically selectable gains implemented in MÖNCH0.4 provided an insight on noise contributors in the front-end designs. By comparing similar designs with minor changes, the effects caused by parasitics have been unveiled as a small reduction of the effective gain and an increase in noise. The design simplification becomes essential to minimise the undesired effects on top of freeing pixel area to optimise the layout including radiation hardening techniques.

The dynamic range is directly linked to the gain. Trade-offs with noise performance are therefore mandatory which leads into needing different designs depending on the type of experiment. The use of DGS architectures, preliminarily tested but not shown in this work, are capable of extending the dynamic range, but the parasitics introduced affect the noise performance for the highest gain settings of the preamplifier. Nonetheless, further investigations will be carried out on the full readout chain of MÖNCH0.4 as well as on the uniform MÖNCH0.3 to further improve the overall performance of future charge integrating HPDs.

The conclusions brought by the characterisation of the ASICs, along readout chain improvements already implemented in JUNGFRÄU and further developments will lead to the design of a new

MÖNCH0.5 prototype. A single pixel design will be implemented in a $4 \times 4 \text{ cm}^2$ (160×160 pixels) prototype in a Multi Project Wafer. The desired architecture is still being discussed and the implementation should be starting at the end of 2023 for an early-2024 MPW run with ASICs available mid-2024. The prototype will be fully characterised in laboratory and used for pilot experiments at beamlines.

These results will validate a candidate for implementation in a full-scale MÖNCH1.0. Two design variants might be required: one for single photon applications with low noise, and one with dynamic gain switching for large dynamic range applications.

Such large devices come with challenges. On the silicon level, where power distribution over such a large area to the high pixel number becomes critical while keeping the total consumption under control. Then, the back-end must also be highly considered as a 1024×768 pixels single chip with static gain operated at 6 kHz will output data at approx. 9.44 GB/s. The volumes of generated raw data will require large storage capabilities. As an example, one hour of operation of the single chip module would fill over 34 TB of disk space. On-the fly data reduction strategies become mandatory. The submission of the up to $3 \times 2 \text{ cm}^2$ chip is currently planned for 2025 with single chip modules available in 2026.

Acknowledgments

This project has received funding from the European Union’s Horizon 2020 research and innovation program under the Marie Skłodowska-Curie grant agreement no. 884104 (PSI-FELLOW-III-3i).

References

- [1] A. Bergamaschi et al., *Looking at single photons using hybrid detectors*, [2015 JINST 10 C01033](#).
- [2] S. Cartier et al., *Micron resolution of MÖNCH and GOTTHARD, small pitch charge integrating detectors with single photon sensitivity*, [2014 JINST 9 C05027](#).
- [3] C. Dullin, J. Albers, G. Tromba, M. Andrä, M. Ramilli and A. Bergamaschi, *MÖNCH detector enables fast and low-dose free-propagation phase-contrast computed tomography of in situ mouse lungs*, [J. Synchrotron Radiat. 25 \(2018\) 565](#).
- [4] M.R. Soman, *High-resolution detectors for soft X-ray spectroscopy*, Ph.D. Thesis, The Open University (2014) [[DOI: 10.21954/OU.RO.0000A424](#)].
- [5] K. Wakonig et al., *X-ray Fourier ptychography*, [Sci. Adv. 5 \(2019\) eaav0282](#).
- [6] S. Cartier et al., *Micrometer-resolution imaging using MÖNCH: towards G_2 -less grating interferometry*, [J. Synchrotron Radiat. 23 \(2016\) 1462](#).
- [7] A. Bergamaschi et al., *The MÖNCH Detector for Soft X-ray, High-Resolution, and Energy Resolved Applications*, [Synchrotron Radiat. News 31 \(2018\) 11](#).
- [8] E. Fröjdth et al., *Detection of MeV electrons using a charge integrating hybrid pixel detector*, [2022 JINST 17 C12004 \[arXiv:2210.16199\]](#).
- [9] R. Dinapoli et al., *MÖNCH, a small pitch, integrating hybrid pixel detector for X-ray applications*, [2014 JINST 9 C05015](#).
- [10] M. Ramilli et al., *Measurements with MÖNCH, a 25 μm pixel pitch hybrid pixel detector*, [2017 JINST 12 C01071](#).
- [11] J. Zhang et al., *Development of LGAD sensors with a thin entrance window for soft X-ray detection*, [2022 JINST 17 C11011 \[arXiv:2210.12993\]](#).